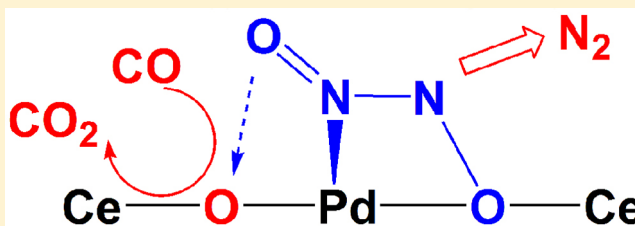


Single Pd Atom Embedded in CeO₂(111) for NO Reduction with CO: A First-Principles Study

Wu-Chen Ding, Xiang-Kui Gu, Hai-Yan Su, and Wei-Xue Li*

State Key Laboratory of Catalysis, Dalian Institute of Chemical Physics, Chinese Academy of Science, Dalian 116023, China

ABSTRACT: Environmental and economic constraints necessitate further improvement of the activity and selectivity of dispersed Pd, Rh, and Pt metals for use in NO_x reduction. We present here a density functional theory plus *U* study of NO reduction with CO catalyzed by a single Pd₁ atom embedded in CeO₂(111) (noted as Pd₁/CeO₂(111)). The complete catalytic cycle for NO + CO → CO₂ + 1/2N₂, including competitive adsorption of reactants, generation of the oxygen vacancy by CO, formation of N₂O₂* intermediates, scission of N–O bonds, and formation of N₂, is mapped out. The calculations indicate that Pd₁/CeO₂(111) is active and selective toward N₂, in agreement with available experimental literature. The key intermediate N₂O₂* toward N₂ is identified, and the rate-limiting step is the first deoxygenation step of N₂O₂* with a barrier of 1.43 eV. The Pd₁–O_v pair embedded in CeO₂(111) is proposed to be the active site, responsible not only for the formation of N₂O₂* by the reaction of two NO molecules but also for the subsequent two deoxygenation steps to make N₂. Detailed electronic structure analysis indicates that the formation of the Pd₁–O_v pair and the synergetic effect between Pd 4d electron and reducibility of CeO₂ are responsible for the catalytic activity of single Pd atom embedded in ceria.



1. INTRODUCTION

Over the decades, the automotive emission control of pollutants such as nitrogen oxides (NO_x), carbon monoxide (CO), and hydrocarbons (HC) has attracted long-standing attention due to their harmful impact on the environment. The main goal for emission control is to convert the pollutant molecules into benign CO₂, N₂, and H₂O. Now, there are mainly two NO_x technologies for this purpose, NO_x storage-reduction^{1–3} in lean-burn engines, and selective catalytic reaction⁴ in spark ignition engines. NO reduction with CO to form CO₂ and N₂ is a common reaction in both technologies due to its advantage of simultaneous removal of two molecules. To catalyze the reaction, the three-way transition metal catalysts including Rh, Pd, or Pt are widely used.^{4–6} The high cost of these precious metals requires continuous improvement of the atomic efficiency and stability. Recently, atomically dispersed Pd₁, Rh₁, and Pt₁ ions doped with CeO₂^{7–13} were synthesized in the absence of mixed phases by a solution combustion method.¹⁴ These catalysts showed excellent catalytic activity, selectivity, and stability for the reaction of NO with CO at low temperature. In particular, complete conversion and 100% selectivity toward N₂ could be found on Pd₁/CeO₂ at 175 °C, whereas slightly lower selectivity for Rh₁ and Pt₁ on CeO₂ was observed.^{10–12} In contrast, for Al₂O₃ supported Pd particles, the complete conversion was reached typically at 350 °C.¹³ It was believed that the strong-metal support interaction and high activity of the surface lattice oxygen of ceria were essential for the observed activity and selectivity.

There has been an increasing amount of interest for the development of catalysts with high specific activity on

heterogeneous supports to improve the cost effectiveness of NO_x reduction catalysts. For instance, this can be achieved by gradually shrinking the size of the supported catalysts, assuming no loss of the intrinsic activity and stability.^{15,16} Actually, small metal clusters or even single atoms were reported to have even higher intrinsic catalytic reactivity than their large particle counterparts.^{17–20} For example, single Pt atoms embedded in the surface of γ-Al₂O₃²¹ and iron oxides²² were attributed to be responsible for the observed low temperature activity of CO oxidation. Moreover, single Pt atoms stabilized by alkali ion clusters could catalyze the low temperature water gas shift reaction (WGS).²³ Iridium was also reported to have remarkably higher WGS activity when it was atomically dispersed on iron oxides.²⁴ Atomically dispersed Ir accounted for ~70% of the total activity of catalysts containing single atoms, subnano clusters, and nanoparticles, thus serving as the most important active sites.

Theoretical studies of oxidation catalysis by atomically dispersed atoms on oxide hosts were recently reviewed by McFarland and Metiu.²⁵ In this work, the single metal cation substituting the cations of an oxide host was found to have a great influence on the formation energy of the oxygen vacancy of the oxide hosts. Moreover, the ease of formation of various dopant–oxide pairs with distinct oxygen activities, depending on the relative valence of the dopants and the reducibility of the host oxides, was concluded to be responsible for the catalytic versatility of the doped oxides for various oxidation reactions. For doped CeO₂ surfaces, density functional theory (DFT)

Received: January 5, 2014

calculations on CO/NO adsorption,^{26–30} CO oxidation,^{31,32} CH₄ oxidation,³³ and CO₂ methanation³⁴ have also been reported.

Despite extensive studies so far, mechanistic understanding of the full reaction for NO + CO → 1/2N₂ + CO₂ on Pd₁-doped ceria is not available. We note that in this catalytic reaction, a number of distinct elementary steps, for instance, competitive adsorption of two reactants, activity of lattice oxygen and role of oxygen vacancy, formation of N–N bond and corresponding intermediate, and scission of N–O bond, might be involved. It remains open whether the single Pd₁ atom embedded in ceria or the lattice oxygen modified by Pd₁ alone could catalyze all of these distinct elementary steps. To address these questions, we present here DFT calculations on a single Pd₁ atom embedded in CeO₂(111) for NO reduction with CO.

2. THEORETICAL APPROACHES AND COMPUTATIONAL DETAILS

Spin-polarized total energy calculations were performed based on the all-electron projected augmented wave (PAW) method and DFT+*U* methodology within the generalized gradient approximation (GGA-PW91) functional as implemented in the Vienna Ab Initio Simulation Package (VASP).^{35–38} A cutoff of 400 eV was used for the plane wave expansion. *U* = 5 eV was applied to Ce 4f states, in line with previous calculations.^{28,33,39} The oxide surface was modeled via a CeO₂(111)-p(3×3) supercell with a thickness of three O–Ce–O trilayers (27 Ce atoms and 54 O atoms overall) separated by a 15 Å vacuum. For the surface Brillouin zone sampling, we employed a Monkhorst–Pack (1×1×1) Γ -centered *k*-points grid.^{32,40} The calculation based on the Monkhorst–Pack of (2×2×1) only lowers the total energy to less than 0.02 eV. The top two trilayers and the adsorbates were relaxed until the residual force on each ion was less than 0.02 eV Å⁻¹.

To simulate Pd₁/CeO₂(111) catalyst, one surface Ce cation was substituted by a Pd₁ atom. Adsorption and reaction was performed on one side of the exposed surface with substituted Pd₁ atom, and the dipole moment correction along the *z* direction was applied. The climbing-image nudged elastic band (CI-NEB) method^{41,42} was used to search the transition states (TSs) for all of the elementary reactions studied. The minimum energy pathway for each elementary reaction was discretized by a total of six images between the initial and final states. The TS was denoted by the highest image along the minimum energy path. The activation energy (*E*_a) of each elementary reaction was calculated by the energy difference between the TS and the initial state (IS) without inclusion of the zero-point energy.

3. RESULTS

3.1. CeO₂(111) and Pd₁/CeO₂(111) Surfaces. The calculated lattice parameter of bulk CeO₂ was 5.49 Å, which agrees well with a previous calculation.³⁰ In this study, we use the CeO₂(111) surface as the support because it is the most abundant surface facet exposed on pristine CeO₂.⁴³ Each surface Ce atom coordinates with seven oxygen atoms, and the optimized Ce–O bond length is 2.37 Å. For the optimized Pd₁/CeO₂(111) (Figure 1), corresponding bond lengths of the surface Ce–O adjacent to Pd atom are 2.39 and 2.40 Å, respectively. The bond length of Pd–O is ~2.23 Å, which is shorter than that of Ce–O, due to the smaller atomic radius of Pd. The calculated formation energy of a bulk Pd atom occupying a pre-existing Ce vacancy is highly exothermic with a

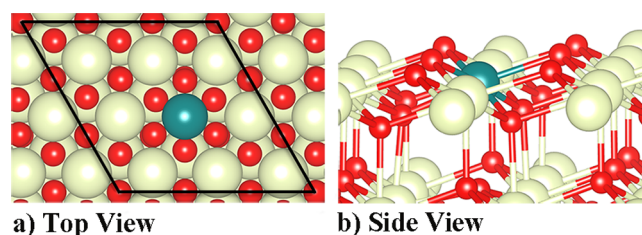


Figure 1. Schematic structure model (top and side views) for Pd₁/CeO₂(111), in which the single Pd₁ atom (dark blue) substitutes the surface Ce cation. The gray and red spheres represent the Ce atom and O atom, respectively.

value of –3.66 eV. This suggests that the substituted Pd₁ atom is stable and would be resistant to the segregation and agglomeration toward metal particles. The high coordination number of substituted Pd₁ atom with lattice oxygen O_L is decisive to its stability and cationic charge state.

We calculated the formation energy of the surface Ce vacancy in CeO₂(111). The corresponding value is 18.91 eV with respect to an isolated Ce atom in the gas phase, which could however be lowered dramatically further if considering formation of Ce bulk metal or other compounds. Nevertheless, the result indicates the formation of the Ce vacancy would be highly activated, a fact that is corroborated by the hashing experimental procedure employed in preparing the corresponding Pd doped ceria oxide.^{7–13} The complete phase diagram of Pd–CeO₂(111) under relevant condition was studied thoroughly by Janik and co-workers⁴⁴ using ab initio thermodynamics. In that work, a number of configurations including Pd₁ adatoms and Pd₄ clusters on CeO₂(111), Pd₁ substituted at the surface Ce sites, and Pd₁ at the subsurface sites were studied, and their relative stabilities were compared to those of Pd bulk metal and oxides. They found that Pd was only favorable as single atoms as either adatoms on the surface or substituted with the surface Ce sites under a wide range of oxygen chemical potential. In particular, they concluded that at 500 K, oxygen partial pressures below atmospheric were sufficient to stabilize the Pd₁ atom substituted with the surface Ce sites, whereas at room temperature, it only required oxygen partial pressure above 10⁻¹⁰ atm. Accordingly, the Pd₁ atom substituted at the surface Ce sites was used throughout the present work without mention otherwise.

The calculated formation energy *E*_V of the oxygen vacancy O_V with respect to O₂ in the gas phase is 2.14 eV (endothermic), which is in good agreement with previous works,^{45,46} and indicates the higher activity of the lattice oxygen O_L and the reducibility of CeO₂(111). The presence of the substituted Pd₁ atom lowers *E*_V of the oxygen vacancy adjacent to Pd₁ to 0.65 eV, which is 1.49 eV smaller than that of the pristine one due to the lower valence of Pd than that of Ce.²⁵ Consequently, the corresponding O_L coordinated with Pd₁ becomes more reactive than the undoped surface.

3.2. Adsorption of CO and NO. A number of the adsorption sites and configurations for CO and NO on CeO₂(111) and Pd₁/CeO₂(111) were explored, and only the results for the most stable sites are given below. Because the oxygen vacancy in ceria plays an important role in catalysis and its concentration could be increased further in the presence of CO and Pd₁, the adsorption on both surfaces in the presence of O_V, noted as O_V/CeO₂(111) and Pd₁-O_V/CeO₂(111) hereafter, was also considered.

On CeO₂(111), calculated binding energies E_b for CO and NO are -0.19 and -0.16 eV, respectively, in good agreement with the previous calculations.^{47–49} The optimized CO and NO configurations are not sensitive to the adsorption sites and were bound at least 2.77 Å away from the CeO₂(111) surface, indicating physical adsorption. On O_v/CeO₂(111), CO binding to the surface is similar to E_b of -0.27 eV. However, NO can bind stronger to the surface via N-end and O-end at O_v, and the calculated E_b values are -0.99 and -0.75 eV, respectively. In other words, NO can only adsorb at the oxygen vacancy of CeO₂(111), whereas CO cannot adsorb on CeO₂(111) irrespective of the presence or absence of an oxygen vacancy.

The presence of the Pd₁ atom embedded in the surface layer of CeO₂(111) dramatically changes the chemistry of the corresponding oxide surface by providing the sites for CO and NO adsorption. On Pd₁/CeO₂(111), CO adsorbs perpendicularly via C-end atop Pd₁(Pd₁-top) with E_b of -0.45 eV (Figure 2a). No stable configuration for NO at Pd₁-top was found.

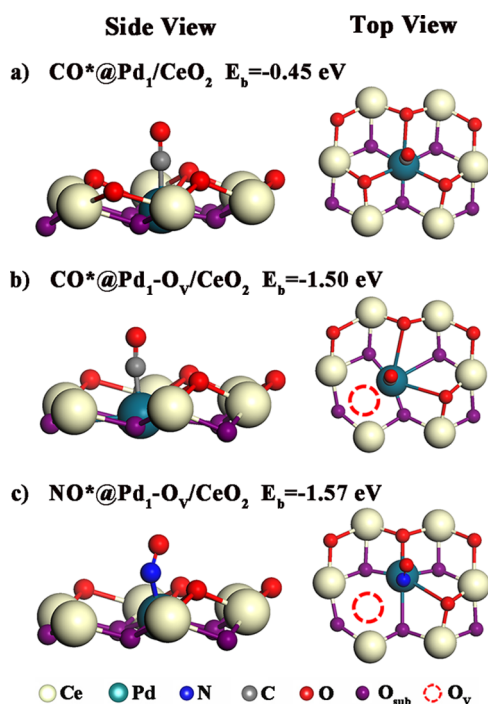


Figure 2. Optimized adsorption structures (side and top views) and binding energies (in eV) of CO* on Pd₁/CeO₂(111) (a) and Pd₁-O_v/CeO₂(111) (b), and NO* on Pd₁-O_v/CeO₂(111) (c) surfaces.

However, when there is O_v adjacent to Pd₁ atom forming a Pd₁-O_v pair, CO adsorption at Pd₁-top is strengthened considerably, and the calculated E_b is -1.50 eV (Figure 2b), whereas CO adsorption via O-end configuration at O_v is unstable. NO adsorption via N-end at Pd₁-top is bound even stronger with E_b of -1.57 eV, and the Pd₁-N bond is tilted 25° away from the normal direction (Figure 2c). The slightly stronger binding of NO adsorption means that the corresponding adsorption is preferential to that of CO. NO adsorption via O-end at O_v is energetically less favorable with a calculated E_b of -0.30 eV, and NO parallel adsorption forming a Pd-O-N-O ring-like structure was also tested but found to be unstable.

Under realistic conditions, the presence of water vapor could hydroxylate the corresponding oxide surfaces, a fact that may influence the corresponding reactivity. To validate the structural model used in above, we examined the influence of

the hydroxylated Pd₁/CeO₂(111) surfaces by introducing a hydrogen on top of oxygen atom adjacent to Pd₁. For hydroxylated Pd₁/CeO₂(111), the calculated formation energy of oxygen vacancy E_v and binding energy E_b for NO adsorption via N-end at Pd₁-top were 0.77 and -1.86 eV, whereas they were 0.65 and -1.57 eV for Pd₁/CeO₂(111), respectively. As compared to E_v (2.14 eV) and E_b (-0.16 eV) for NO binding on CeO₂(111), decrease of formation energy of oxygen vacancy and increase of binding strength of NO at Pd₁-top on hydroxylated Pd₁/CeO₂(111) are essentially the same as those on Pd₁/CeO₂(111).

3.3. CO Oxidation. Having studied the adsorption of NO and CO, we then explored CO oxidation with O_L to form O_v, which is important for the subsequent reduction of NO. For CeO₂(111), because CO binds weakly to the surface, the Eley–Rideal (E–R) type of reaction mechanism was investigated, and the calculated potential energy surfaces are shown in Figure 3.

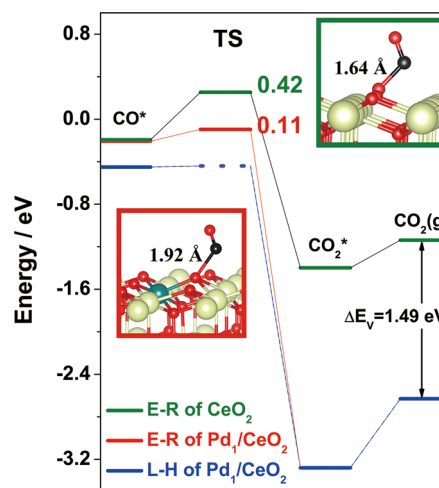


Figure 3. Potential energy surfaces for CO oxidation with surface lattice oxygen via Eley–Rideal (E–R) mechanism on CeO₂(111) (green) and Pd₁/CeO₂(111) (red), and Langmuir–Hinshelwood (L–H) mechanism on Pd₁/CeO₂(111) (blue). Corresponding transition states (TSs), bond length of new chemical bond formed between CO and lattice oxygen (in Å), and the activation barrier with respect to the initial state (in eV) are indicated. “*” and “g” represent the species on surfaces and in the gas phase, and $\Delta E_v = 1.49$ eV is the difference in formation energy of oxygen vacancy between Pd₁/CeO₂(111) and CeO₂(111).

The elementary reaction energy between CO in the gas phase (right on top of O_L) and O_L to form CO₂* at the surface is exothermic by -1.21 eV, and with a modest barrier of 0.42 eV. At the TS (Figure 3, green frame), corresponding O_L is slightly pulled up from the surface, and the bond length between C of CO and O_L is 1.64 Å. The calculated binding energy of the formed CO₂* with respect to the surface underneath is -0.26 eV, meaning that desorption of CO₂* with an O_v left behind is facile.

On Pd₁/CeO₂(111), the calculated reaction energy to form CO₂* is exothermic by -3.08 eV, with a small barrier of 0.11 eV via E–R reaction pathway. As compared to CO oxidation on CeO₂(111) with a reaction energy of -1.21 eV, the more exothermic reaction energy on Pd₁/CeO₂(111) comes from its smaller energy cost to consume the corresponding lattice oxygen O_L, whose formation energy of oxygen vacancy E_v is 1.49 eV lower than that of CeO₂(111). The optimized TS is

shown schematically in Figure 3 (red frame). The larger C–O distance between C and lattice O (1.92 Å) required to reach the TS than that of CeO₂(111) (1.64 Å) rationalizes its smaller barrier (0.11 eV versus 0.42 eV). Besides the E–R mechanism, the Langmuir–Hinshelwood (L–H) mechanism was also considered; CO first adsorbs at Pd₁-top and reacts with O_L afterward. This process is nearly barrierless with the reaction energy of –2.83 eV, as shown in Figure 3 (blue frame). The formed CO₂* (the common final state for both pathways) could desorb from the Pd₁/CeO₂(111) with a modest energy cost of 0.65 eV, leaving a Pd₁–O_V pair behind. As compared to the E–R mechanism, it can be found that the L–H mechanism is more favorable for CO oxidation on Pd₁/CeO₂(111).

3.4. N₂O₂ Formation. N₂ formation might arise from the recombination of adsorbed N* atoms from the direct NO dissociation. To test this possibility, we calculated the dissociative reaction energy from gas-phase NO to N* and O* adsorbed at cation-top. For stoichiometric CeO₂(111) and Pd₁/CeO₂(111), the calculated reaction energies are highly endothermic (>6 eV). Even for the reduced surfaces where the presence of O_V might accommodate the dissociated O*, the calculated reaction energies remain very endothermic, 1.95 eV for O_V/CeO₂(111) and 3.54 eV for Pd₁–O_V/CeO₂(111). These results indicate that direct NO dissociation into N* and O* hardly contributes to N₂ formation, if at all, on either stoichiometric or reduced CeO₂(111) and Pd₁/CeO₂(111).

Alternatively, N₂ formation might arise from formation of the N₂O₂* intermediate from two NO* molecules adsorbed on the surfaces, followed by the sequential scission of the N–O bonds. To test this pathway, we start from perfect CeO₂(111) for reference again. Because the NO binding on CeO₂(111) is weak, the formation of the N₂O₂* intermediate via the combination between adsorbed NO* on CeO₂(111) would be limited. On the other hand, in the presence of O_V, NO might bind considerably to O_V. However, as found in the above calculations, the favorable configuration for NO adsorption at O_V is the N-end configuration. Thus, the N atom is not accessible to the coming NO, which will prevent the formation of the N–N bond. In other words, the formation of the N–N bond via N₂O₂* intermediate from coadsorbed NO* molecules on CeO₂(111) is unlikely, even in the presence of O_V.

N₂O₂* could however be formed on Pd₁–O_V/CeO₂(111) in the presence of the Pd₁–O_V pairs. As found above, the Pd₁–O_V pair tends to bind the NO via N-end at the Pd₁-top site, and the corresponding binding energy calculated is –1.57 eV (Figure 4). CO binding at the Pd₁-top site is slightly unfavorable with a binding energy of –1.50 eV. Once NO adsorbs the Pd₁-top site, the adjacent O_V remains able to accommodate molecules such as NO and CO. NO adsorption at O_V was found to preferential adsorption via O-end at the O_V site, and its high-lying N atom points toward the low-lying N atom of the NO already at the Pd₁-top site, forming N–N bond with a bond length of 1.18 Å. The formation of the new N–N bond stabilizes the coming NO, and the corresponding energy gain calculated is –1.31 eV. For CO adsorption at O_V, however, the corresponding energy gain by formation of ONCO* intermediate is –0.07 eV only, which cannot compete with NO adsorption at O_V. This leads preferentially to the formation of N₂O₂* intermediate from two NO molecules with an overall energy gain of –2.88 eV. As shown schematically in Figure 4, N₂O₂* intermediate locates at the Pd₁–O_V pairs, one binding via the N atom to a Pd₁-top site and the other binding via the O atom to an oxygen vacancy adjacent the Pd₁ atom.

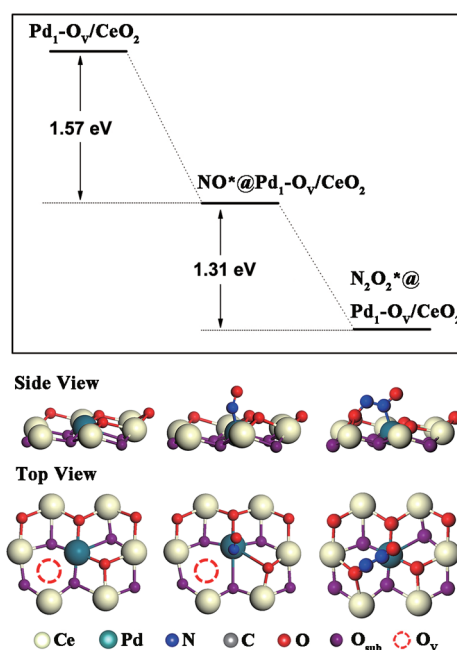


Figure 4. Potential energy surface for the formation of N₂O₂* intermediate from the sequential adsorption of two NO molecules on Pd₁–O_V/CeO₂(111), and the corresponding structures (side and top views) are shown schematically at the bottom.

We estimate the reaction barrier for formation of N₂O₂* is small or even negligible. However, this estimation should be treated with caution, due to the difficulty in proper description of the spin crossing⁵⁰ involved in this particular process. We note that the ground state for isolated NO in the gas phase, individual NO* adsorbed at Pd₁-top sites, and O_V sites separately all have a finite magnetic moment (about 1 μ_B), whereas the ground state for N₂O₂ in the gas phase and N₂O₂* on ceria surfaces is a singlet state only with 0 μ_B. Fortunately, we found that before the formation of N–N bond and N₂O₂*, there are two degenerate states, which have nearly the same energetics and geometries but distinct spin states, 1.7 and 0 μ_B. These degenerated states would facilitate greatly spin crossing. Once it transits from a high spin state to a singlet state, it would be an energetically downhill process toward the final product of N₂O₂* without any barrier based on single state NEB calculation.

3.5. N₂O₂ Decomposition and N₂ Formation. Decomposition of the N₂O₂* intermediate on Pd₁–O_V/CeO₂(111) via the scission of two N–O bonds and Pd₁–N bond would lead to the desired product of N₂. The first reaction pathway (I) calculated for this purpose is shown in Figure 5. In this pathway, the Pd₁–N bond breaks first by overcoming a barrier of 1.37 eV (TS2, Figure 5). This leads to the formation of a linear O–N–N–O* intermediate with O-end at the O_V site, and the corresponding reaction energy is endothermic with a value of 1.23 eV. Subsequent scission of the lower N–O bond requires overcoming a barrier of 0.64 eV (TS3, Figure 5) with an energy gain of 0.89 eV. The corresponding N–O bond length at TS3 is 1.70 Å. This step produces a gaseous N₂O and leaves one oxygen behind filling the O_V, and Pd₁/CeO₂(111) surface is recovered accordingly. The overall barrier and the corresponding reaction energy from N₂O₂* on Pd₁–O_V/CeO₂(111) to gaseous N₂O and Pd₁/CeO₂(111) are 1.85 and 0.34 eV (endothermic). We note that the gaseous N₂O could

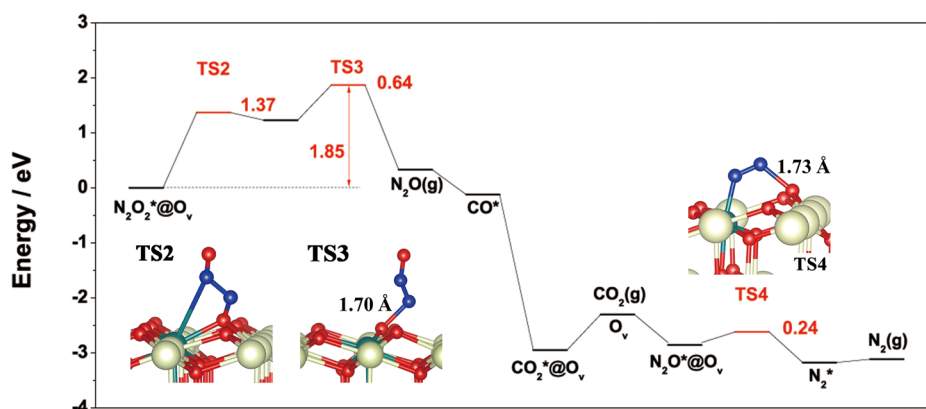


Figure 5. Potential energy surface (pathway I) for decomposition of N_2O_2^* intermediate toward N_2 on $\text{Pd}_1\text{-O}_V/\text{CeO}_2(111)$. Corresponding TS for TS2, TS3, and TS4 with critical bond lengths at TS (in Å) and elementary reaction barriers (eV) are also given. The white, dark cyan, gray, blue, and red spheres represent Ce, Pd, C, N, and O atoms, respectively.

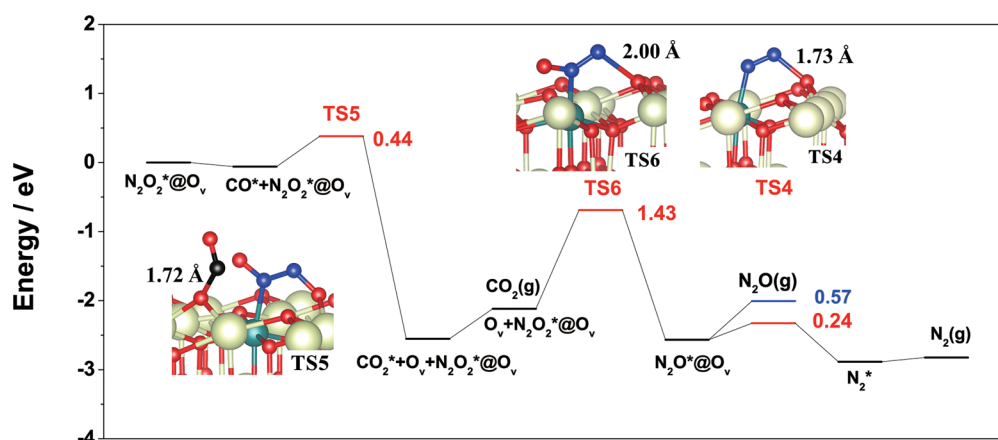


Figure 6. Potential energy surface (pathway II) for decomposition of N_2O_2^* intermediate toward N_2 on $\text{Pd}_1\text{-O}_V/\text{CeO}_2(111)$. Corresponding TS for TS4, TS5, and TS6 with critical bond lengths at TS (in Å) and elementary reaction barriers (eV) are also given. The white, dark cyan, gray, blue, and red spheres represent Ce, Pd, C, N, and O atoms, respectively.

also be produced by simultaneous scission of the $\text{Pd}_1\text{-N}$ bond and N-O bond at O_V . This process is however kinetically less favorable because of its slightly higher barrier of 1.96 eV calculated.

The formation of the gaseous N_2O would lower the selectivity of N_2 , and further reduction is necessary. N_2O adsorption on $\text{Pd}_1/\text{CeO}_2(111)$ is limited due to its weak binding to Pd_1/CeO_2 (-0.07 eV). However, as shown in Figure 3 and incorporated in Figure 5, $\text{Pd}_1/\text{CeO}_2(111)$ could be easily reduced by CO and becomes $\text{Pd}_1\text{-O}_V/\text{CeO}_2(111)$. We find that N_2O adsorption via O-end at O_V of $\text{Pd}_1\text{-O}_V/\text{CeO}_2(111)$ is likely with binding energy of -0.57 eV. The subsequent scission of the N-O bond of N_2O^* adsorbed on $\text{Pd}_1\text{-O}_V/\text{CeO}_2(111)$ has a small barrier of 0.24 eV with exothermic reaction energy of 0.45 eV. The N-O bond length at TS is 1.73 Å (TS4, Figure 5). $\text{Pd}_1/\text{CeO}_2(111)$ surface is recovered again. Although the catalytic cycle could be closed with formation of the final product N_2 , the readsorption of the gaseous N_2O would limit the corresponding selectivity.

Another kinetically more favorable reaction pathway (II) from N_2O_2^* on $\text{Pd}_1\text{-O}_V/\text{CeO}_2(111)$ to N_2 is calculated and shown in Figure 6. In this pathway, one O_L adjacent to Pd_1 first reacts with CO in the gas phase to form CO_2^* . The corresponding transition state optimized is shown schematically as TS5 of Figure 6. The barrier and reaction energy are 0.44

and -2.49 eV, respectively. The CO_2^* desorbs quickly due to its weak binding (-0.22 eV) with respect to the substrate underneath and leaves behind an O_V . The high-lying N-O bond of N_2O_2^* with N-end at Pd_1 -top displaces and rotates downward to the generated O_V . The transition state to break the corresponding N-O bond is approached at N-O bond length of 2.00 Å and $\text{Pd}_1\text{-N}$ bond length of 1.99 Å (TS6, Figure 6). The dissociated O fills eventually O_V , and N_2O^* intermediate is formed on $\text{Pd}_1\text{-O}_V/\text{CeO}_2(111)$. The reaction barrier and energy for this step are 1.43 and -0.45 eV, respectively. The binding energy of the resulting N_2O^* with respect to $\text{Pd}_1\text{-O}_V/\text{CeO}_2(111)$ underneath is -0.57 eV, whereas the scission of the N-O bond of N_2O^* to generate gaseous N_2 is facile with a barrier of 0.24 eV only (TS4, Figure 5). Therefore, N_2O^* formed tends to dissociate N-O bond producing N_2 rather than desorb directly to the gas phase.

4. DISCUSSION

The favorable catalytic cycle for $2\text{CO} + 2\text{NO} \rightarrow \text{N}_2 + 2\text{CO}_2$ on $\text{Pd}_1/\text{CeO}_2(111)$ is shown in Figure 7. The main reaction pathway includes the reaction between CO and the lattice oxygen O_L to generate O_V and therefore the $\text{Pd}_1\text{-O}_V$ pair, followed by adsorption of two NO sequentially at Pd_1 -top and adjacent O_V forming N_2O_2^* , generation of O_V by CO again, and sequential scission of two N-O bonds of N_2O_2^* producing

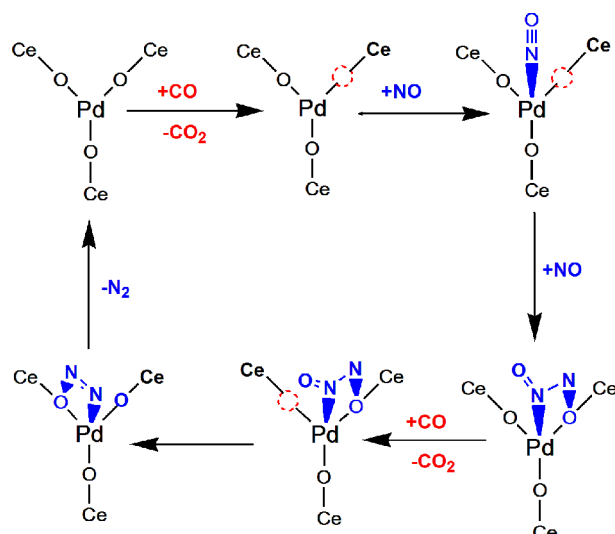


Figure 7. Catalytic cycle derived for the $2\text{NO} + 2\text{CO} \rightarrow \text{N}_2 + 2\text{CO}_2$ reaction on $\text{Pd}_1/\text{CeO}_2(111)$.

N_2 . The rate-limiting step in the catalytic cycle is the scission of the first N–O bond of N_2O^* intermediate with a barrier of 1.43 eV (TS6), and there is no desorption of N_2O^* into the gas phase. These results mean that the overall catalytic cycle optimized is facile and has a high selectivity of N_2 , which is in accord with available experimental findings.^{7–13}

The reaction mechanism revealed on $\text{Pd}_1/\text{CeO}_2(111)$ is rather different from those using supported metal particles as the active catalysts.^{4–11} For the latter one, the metal particles have high surface area, and there are a large number of sites available for adsorption of both CO and NO reactants. NO^* prefers to dissociate directly into N^* and O^* at the low coordination sites (for instance, the step edge⁵¹). N^* dissociated from NO may combine with another N^* to form N_2 directly, or with coadsorbed NO to form N_2O^* followed by the scission of N–O bond to form N_2 .

The distinct reaction pathway between NO and CO reaction on $\text{Pd}_1/\text{CeO}_2(111)$ stems from the formation of active $\text{Pd}_1\text{–O}_V$ pairs embedded in the oxide. The oxygen vacancy O_V in the $\text{Pd}_1\text{–O}_V$ pair acts as the efficient active site for both NO adsorption and the subsequent scission of the N–O bond (TS3, TS4, and TS6). This is possible because of the high activity of the lattice oxygen of $\text{CeO}_2(111)$, the small formation energy of oxygen vacancy (less than 2.14 eV) and lower reaction barrier with CO (less than 0.42 eV).

The Pd_1 cation in the $\text{Pd}_1\text{–O}_V$ pair also plays an essential role in the catalytic cycle. Specifically, it provides the additional adsorption site for NO, the key for the formation of N–N bond, which could not be realized on pure ceria otherwise. The strong chemical binding of CO/NO with the substrates comes from the presence of d valence electrons in Pd_1 not available in Ce, allowing for efficient orbital hybridization. For instance, the charge density difference of CO adsorption at the Pd_1 -top site (Figure 8a) of $\text{Pd}_1/\text{CeO}_2(111)$ shows a pronounced charge accumulation between Pd_1 and CO and the redistribution around Pd_1 and CO. If there is the oxygen vacancy such as on $\text{Pd}_1\text{–O}_V/\text{CeO}_2(111)$ surface, excess electron from O_V transfer partially to the adjacent Pd_1 , for instance, by 0.43 e per O_V according to the calculated Bader charge. This promotes the charge accumulation and redistribution between CO and Pd_1 , as is evident in Figure 8b. Accordingly, the corresponding CO

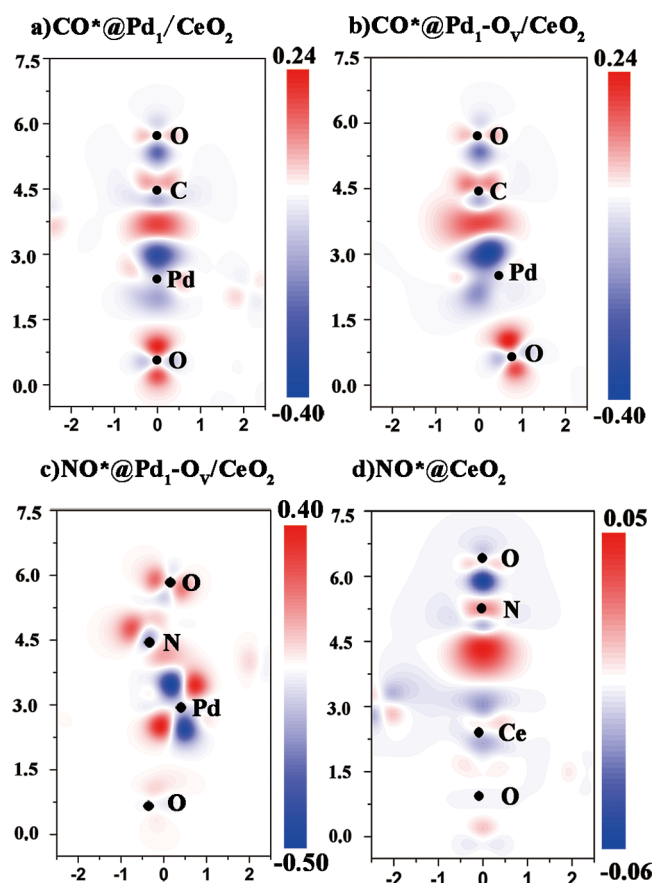


Figure 8. Charge density difference for CO^* adsorption at Pd_1 -top site of $\text{Pd}_1/\text{CeO}_2(111)$ (a) and $\text{Pd}_1\text{–O}_V/\text{CeO}_2(111)$ (b), NO^* adsorption at Pd_1 -top site of $\text{Pd}_1\text{–O}_V/\text{CeO}_2(111)$ (c), and NO^* adsorption on $\text{CeO}_2(111)$ (d). Red and blue colors represent the charge accumulation and depletion (in units of $e/\text{Å}^3$), accordingly.

binding increases significantly from -0.45 to -1.50 eV. A similar occurrence can be found for NO adsorption at the Pd_1 -top site (Figure 8c) of $\text{Pd}_1\text{–O}_V/\text{CeO}_2(111)$ surface, and comprehensive variation in charge density difference is seen. For comparison, the charge density difference for NO adsorption on $\text{CeO}_2(111)$ surface is also shown in Figure 8d. The extent of charge accumulation and redistribution decreases significantly, supporting the finding of the rather weak binding of NO on $\text{CeO}_2(111)$.

The importance of d valence electrons in Pd_1 for strong chemical binding and orbital hybridization with molecule orbitals can be best visualized by projected density of states (PDOS) for NO adsorption at the Pd_1 -top site of $\text{Pd}_1\text{–O}_V/\text{CeO}_2(111)$ and the Ce-top site of $\text{CeO}_2(111)$. For NO/ $\text{Pd}_1\text{–O}_V/\text{CeO}_2(111)$ (Figure 9a), Pd 4d-electrons dominate PDOS below the Fermi level, and the comprehensive orbital hybridization with NO $2\pi^*$ orbital,⁵² formation of bonding and antibonding states below and above the Fermi level, is evidently seen. This rationalizes the large calculated NO binding energy of -1.57 eV. For NO/ $\text{CeO}_2(111)$ (Figure 9b), there are a few electrons below the Fermi level from Ce 5d6s, whereas there is a prominent peak at about 1.5 eV above the Fermi level from Ce 4f, which hybridizes extensively with NO $2\pi^*$ orbital. Because the hybridization occurs mainly at the unoccupied states, the resulted chemical bond is rather weak with a value of -0.16 eV only.

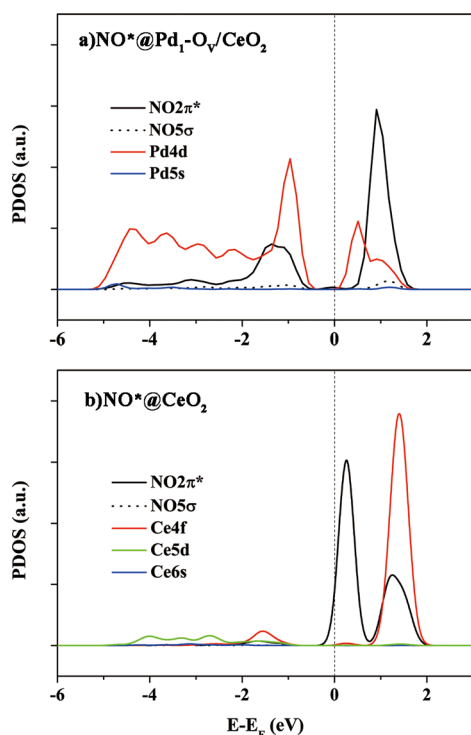


Figure 9. Projected density of states (PDOS) for NO* adsorption at Pd₁-top site of Pd₁-O_V/CeO₂(111) (a) and Ce-top site of CeO₂(111) (b) with respect to Fermi level. Red line represents Pd 4d and/or Ce 4f, blue is for Pd 5s and/or Ce 6s, green is for Ce 5d, black is for NO 2π* from the summation of corresponding p_x and p_y components, and the dotted line is for NO 5σ from the summation of corresponding p_z components, respectively.

5. CONCLUSIONS

In summary, the catalysis of the single Pd₁ atoms embedded in CeO₂(111) for NO and CO reaction is studied using the density functional theory. A number of the elementary reaction steps, including competitive adsorption of reactants, generation of the oxygen vacancy via CO reaction with lattice oxygen, formation of N–N bond, and scission of N–O bonds, are explored. Corresponding potential energy surface and complete catalytic cycle with preferential selectivity toward CO₂ and N₂ are mapped out. In the catalytic cycle, the key intermediate of N₂O₂* toward N₂ by two deoxygenation steps is identified. We found that the scission of the first N–O bond of N₂O₂* intermediate is the rate-limiting step, and the corresponding barrier of 1.43 eV calculated shows that the process is facile. The Pd₁–O_V pair embedded in the ceria surface layer is the active site, as it can accommodate the adsorption of two NO molecules to facilitate formation of the N₂O₂* intermediate and catalyze the subsequent N–O bond scission. The formation of the Pd₁–O_V pair and corresponding synergetic effect between Pd₁ with abundant d-electron and O_V of CeO₂ are key for the corresponding catalysis of the single Pd atom in ceria.

AUTHOR INFORMATION

Corresponding Author

*E-mail: wxli@dicp.ac.cn.

Notes

The authors declare no competing financial interest.

ACKNOWLEDGMENTS

This work was supported by the NSFC (21173210, 21225315), 973 (2013CB834603), and CAS (XDA09030101).

REFERENCES

- (1) Matsumoto, S. i.; Ikeda, Y.; Suzuki, H.; Ogai, M.; Miyoshi, N. NO_x storage-reduction catalyst for automotive exhaust with improved tolerance against sulfur poisoning. *Appl. Catal., B* **2000**, *25*, 115–124.
- (2) Liu, G.; Gao, P.-X. A review of NO_x storage/reduction catalysts: mechanism, materials and degradation studies. *Catal. Sci. Technol.* **2011**, *1*, 552–568.
- (3) Epling, W. S.; Campbell, L. E.; Yezerets, A.; Currier, N. W.; Parks, J. E. Overview of the fundamental reactions and degradation mechanisms of NO_x storage/reduction catalysts. *Catal. Rev.* **2004**, *46*, 163–245.
- (4) Srinivasan, A.; Depcik, C. Review of chemical reactions in the NO reduction by CO on rhodium/alumina catalysts. *Catal. Rev.* **2010**, *52*, 462–493.
- (5) Pisanu, A. M.; Gigola, C. E. NO decomposition and NO reduction by CO over Pd/α-Al₂O₃. *Appl. Catal., B* **1999**, *20*, 179–189.
- (6) Szailer, T.; Kwak, J. H.; Kim, D. H.; Hanson, J. C.; Peden, C. H. F.; Szanyi, J. Reduction of stored NO_x on Pt/Al₂O₃ and Pt/BaO/Al₂O₃ catalysts with H₂ and CO. *J. Catal.* **2006**, *239*, 51–64.
- (7) Bera, P.; Patil, K. C.; Jayaram, V.; Subbanna, G. N.; Hegde, M. S. Ionic dispersion of Pt and Pd on CeO₂ by combustion method: Effect of metal–ceria interaction on catalytic activities for NO reduction and CO and hydrocarbon oxidation. *J. Catal.* **2000**, *196*, 293–301.
- (8) Baidya, T.; Priolkar, K. R.; Sarode, P. R.; Hegde, M. S.; Asakura, K.; Tateno, G.; Koike, Y. Local structure of Pt and Pd ions in Ce_{1-x}Ti_xO₂: X-ray diffraction, x-ray photoelectron spectroscopy, and extended x-ray absorption fine structure. *J. Chem. Phys.* **2008**, *128*, 124711.
- (9) Priolkar, K. R.; Bera, P.; Sarode, P. R.; Hegde, M. S.; Emura, S.; Kumashiro, R.; Lalla, N. P. Formation of Ce_{1-x}Pd_xO_{2-δ} solid solution in combustion-synthesized Pd/CeO₂ catalyst: XRD, XPS, and EXAFS investigation. *Chem. Mater.* **2002**, *14*, 2120–2128.
- (10) Bera, P.; Hegde, M. S. NO reduction over noble metal ionic catalysts. *Catal. Surv. Asia* **2011**, *15*, 181–199.
- (11) Roy, S.; Hegde, M. S. Pd ion substituted CeO₂: A superior de-NO_x catalyst to Pt or Rh metal ion doped ceria. *Catal. Commun.* **2008**, *9*, 811–815.
- (12) Roy, S.; Marimuthu, A.; Hegde, M. S.; Madras, G. High rates of NO and N₂O reduction by CO, CO and hydrocarbon oxidation by O₂ over nano crystalline Ce_{0.98}Pd_{0.02}O_{2-δ}: Catalytic and kinetic studies. *Appl. Catal., B* **2007**, *71*, 23–31.
- (13) Baidya, T.; Marimuthu, A.; Hegde, M. S.; Ravishankar, N.; Madras, G. Higher catalytic activity of nano-Ce_{1-x-y}Ti_xPd_yO_{2-δ} compared to nano-Ce_{1-x}Pd_xO_{2-δ} for CO oxidation and N₂O and NO reduction by CO: Role of oxide ion vacancy. *J. Phys. Chem. C* **2006**, *111*, 830–839.
- (14) Hegde, M. S.; Madras, G.; Patil, K. C. Noble metal ionic catalysts. *Acc. Chem. Res.* **2009**, *42*, 704–712.
- (15) Valden, M.; Lai, X.; Goodman, D. W. Onset of catalytic activity of gold clusters on titania with the appearance of nonmetallic properties. *Science* **1998**, *281*, 1647–1650.
- (16) Van Santen, R. A. Complementary structure sensitive and insensitive catalytic relationships. *Acc. Chem. Res.* **2008**, *42*, 57–66.
- (17) Herzing, A. A.; Kiely, C. J.; Carley, A. F.; Landon, P.; Hutchings, G. J. Identification of active gold nanoclusters on iron oxide supports for CO oxidation. *Science* **2008**, *321*, 1331–1335.
- (18) Turner, M.; Golovko, V. B.; Vaughan, O. P. H.; Abdulkin, P.; Berenguer-Murcia, A.; Tikhov, M. S.; Johnson, B. F. G.; Lambert, R. M. Selective oxidation with dioxygen by gold nanoparticle catalysts derived from 55-atom clusters. *Nature* **2008**, *454*, 981–983.
- (19) Vajda, S.; Pellin, M. J.; Greeley, J. P.; Marshall, C. L.; Curtiss, L. A.; Ballentine, G. A.; Elam, J. W.; Catillon-Mucherie, S.; Redfern, P. C.; Mehmood, F.; Zapol, P. Subnanometre platinum clusters as highly

active and selective catalysts for the oxidative dehydrogenation of propane. *Nat. Mater.* **2009**, *8*, 213–216.

(20) Judai, K.; Abbet, S.; Wörz, A. S.; Heiz, U.; Henry, C. R. Low-temperature cluster catalysis. *J. Am. Chem. Soc.* **2004**, *126*, 2732–2737.

(21) Kwak, J. H.; Hu, J.; Mei, D.; Yi, C.-W.; Kim, D. H.; Peden, C. H. F.; Allard, L. F.; Szanyi, J. Coordinatively unsaturated Al³⁺ centers as binding sites for active catalyst phases of platinum on γ -Al₂O₃. *Science* **2009**, *325*, 1670–1673.

(22) Qiao, B. T.; Wang, A. Q.; Yang, X. F.; Allard, L. F.; Jiang, Z.; Cui, Y. T.; Liu, J. Y.; Li, J.; Zhang, T. Single-atom catalysis of CO oxidation using Pt₁/FeO_x. *Nat. Chem.* **2011**, *3*, 634–641.

(23) Zhai, Y.; Pierre, D.; Si, R.; Deng, W.; Ferrin, P.; Nilekar, A. U.; Peng, G.; Herron, J. A.; Bell, D. C.; Saltsburg, H.; Mavrikakis, M.; Flytzani-Stephanopoulos, M. Alkali-stabilized Pt-OH_x species catalyze low-temperature water-gas shift reactions. *Science* **2010**, *329*, 1633–1636.

(24) Lin, J.; Wang, A.; Qiao, B.; Liu, X.; Yang, X.; Wang, X.; Liang, J.; Li, J.; Liu, J.; Zhang, T. Remarkable performance of Ir₁/FeO_x single-atom catalyst in water gas shift reaction. *J. Am. Chem. Soc.* **2013**, *135*, 15314–15317.

(25) McFarland, E. W.; Metiu, H. Catalysis by doped oxides. *Chem. Rev.* **2013**, *113*, 4391–4427.

(26) Nolan, M. Enhanced oxygen vacancy formation in ceria (111) and (110) surfaces doped with divalent cations. *J. Mater. Chem.* **2011**, *21*, 9160–9168.

(27) Nolan, M. Charge transfer and formation of reduced Ce³⁺ upon adsorption of metal atoms at the ceria (110) surface. *J. Chem. Phys.* **2012**, *136*, 134703.

(28) Nolan, M. Molecular adsorption on the doped (110) ceria surface. *J. Phys. Chem. C* **2009**, *113*, 2425–2432.

(29) Nolan, M.; Verdugo, V. S.; Metiu, H. Vacancy formation and CO adsorption on gold-doped ceria surfaces. *Surf. Sci.* **2008**, *602*, 2734–2742.

(30) Yang, Z.; Woo, T. K.; Hermansson, K. Adsorption of NO on unreduced and reduced CeO₂ surfaces: A plane-wave DFT study. *Surf. Sci.* **2006**, *600*, 4953–4960.

(31) Chen, H.-T. First-principles study of CO adsorption and oxidation on Ru-doped CeO₂(111) surface. *J. Phys. Chem. C* **2012**, *116*, 6239–6246.

(32) Shapovalov, V.; Metiu, H. Catalysis by doped oxides: CO oxidation by Au_xCe_{1-x}O₂. *J. Catal.* **2007**, *245*, 205–214.

(33) Mayernick, A. D.; Janik, M. J. Methane oxidation on Pd–ceria: A DFT study of the mechanism over Pd_xCe_{1-x}O₂, Pd, and PdO. *J. Catal.* **2011**, *278*, 16–25.

(34) Sharma, S.; Hu, Z.; Zhang, P.; McFarland, E. W.; Metiu, H. CO₂ methanation on Ru-doped ceria. *J. Catal.* **2011**, *278*, 297–309.

(35) Kresse, G.; Furthmüller, J. Efficiency of ab-initio total energy calculations for metals and semiconductors using a plane-wave basis set. *Comput. Mater. Sci.* **1996**, *6*, 15–50.

(36) Kresse, G.; Furthmüller, J. Efficient iterative schemes for ab initio total-energy calculations using a plane-wave basis set. *Phys. Rev. B* **1996**, *54*, 11169.

(37) Kresse, G.; Hafner, J. Ab initio molecular-dynamics simulation of the liquid-metal&amorphous-semiconductor transition in germanium. *Phys. Rev. B* **1994**, *49*, 14251.

(38) Kresse, G.; Hafner, J. Ab initio molecular dynamics for open-shell transition metals. *Phys. Rev. B* **1993**, *48*, 13115.

(39) Nolan, M. Charge compensation and Ce³⁺ formation in trivalent doping of the CeO₂(110) surface: The key role of dopant ionic radius. *J. Phys. Chem. C* **2011**, *115*, 6671–6681.

(40) Nolan, M. Healing of oxygen vacancies on reduced surfaces of gold-doped ceria. *J. Chem. Phys.* **2009**, *130*, 144702.

(41) Henkelman, G.; Uberuaga, B. P.; Jonsson, H. A climbing image nudged elastic band method for finding saddle points and minimum energy paths. *J. Chem. Phys.* **2000**, *113*, 9901–9904.

(42) Henkelman, G.; Jonsson, H. Improved tangent estimate in the nudged elastic band method for finding minimum energy paths and saddle points. *J. Chem. Phys.* **2000**, *113*, 9978–9985.

(43) Skorodumova, N.; Baudin, M.; Hermansson, K. Surface properties of CeO₂ from first principles. *Phys. Rev. B* **2004**, *69*, 075401.

(44) Mayernick, A. D.; Janik, M. J. Ab initio thermodynamic evaluation of Pd atom interaction with CeO₂ surfaces. *J. Chem. Phys.* **2009**, *131*, 084701.

(45) Li, H.-Y.; Wang, H.-F.; Gong, X.-Q.; Guo, Y.-L.; Guo, Y.; Lu, G.; Hu, P. Multiple configurations of the two excess 4f electrons on defective CeO₂(111): Origin and implications. *Phys. Rev. B* **2009**, *79*, 193401.

(46) Ganduglia-Pirovano, M.; Da Silva, J.; Sauer, J. Density-functional calculations of the structure of near-surface oxygen vacancies and electron localization on CeO₂(111). *Phys. Rev. Lett.* **2009**, *102*, 026101.

(47) Huang, M.; Fabris, S. CO adsorption and oxidation on ceria surfaces from DFT+U calculations. *J. Phys. Chem. C* **2008**, *112*, 8643–8648.

(48) Nolan, M.; Parker, S. C.; Watson, G. W. CeO₂ catalyzed conversion of CO, NO₂ and NO from first principles energetics. *Phys. Chem. Chem. Phys.* **2006**, *8*, 216–218.

(49) Hsu, L.-C.; Tsai, M.-K.; Lu, Y.-H.; Chen, H.-T. Computational investigation of CO adsorption and oxidation on Mn/CeO₂(111) surface. *J. Phys. Chem. C* **2012**, *117*, 433–441.

(50) Chrétien, S.; Metiu, H. O₂ evolution on a clean partially reduced rutile TiO₂(110) surface and on the same surface precovered with Au₁ and Au₂: The importance of spin conservation. *J. Chem. Phys.* **2008**, *129*, 074705.

(51) Hammer, B. Bond activation at monatomic steps: NO dissociation at corrugated Ru(0001). *Phys. Rev. Lett.* **1999**, *83*, 3681–3684.

(52) Zeng, Z.-H.; Da Silva, J. L. F.; Li, W.-X. Theory of nitride oxide adsorption on transition metal (111) surfaces: a first-principles investigation. *Phys. Chem. Chem. Phys.* **2010**, *12*, 2459–2470.